Bicrystalline Zn_3P_2 and Cd_3P_2 Nanobelts and Their Electronic Transport Properties

Guozhen Shen,*,† Po-Chiang Chen,† Yoshio Bando,‡ Dmitri Golberg,‡,§ and Chongwu Zhou*,†

Department of Electrical Engineering, University of Southern California, Los Angeles, California 90089, and World Premier International Center for Materials Nanoarchitectonics (MANA) and Nanoscale Materials Center, National Institute for Materials Science, Namiki 1-1, Tsukuba, Ibaraki 305-0044, Japan

Received September 16, 2008. Revised Manuscript Received October 7, 2008

As an interesting morphology and phase, the 1D bicrystalline (twinned) nanostructures have received much consideration because of their peculiar structure. In this paper, bicrystal nanobelts of Zn_3P_2 and Cd_3P_2 have been prepared on a large scale, via a simple vapor-solid process. The products were characterized using X-ray diffraction, scanning electron microscopy, transmission electron microscopy, as well as energy-dispersive X-ray spectrometer and the results revealed that both of them are of bicrystal shapes with the preferred growth axis along the [101] directions. P-type Field-effect transistors (FETs) based on single Zn_3P_2 and Cd_3P_2 nanobelts were fabricated, which revealed the thermal activation of carriers as the dominant transport mechanism, as was verified under the measurements at various temperatures (100−300 K).

1. Introduction

Synthesis and assembly of nanostructures with special morphologies, shapes, and compositions have attracted great interests in recent years because of their interesting physical and chemical properties associated with their specific characteristics. Many kinds of interesting nanostructures, such as 1D nanowires, nanobelts, 3D patterns, hierarchical structures and heterostructures, and 2D superlattices, have been produced using many kinds of methods based on the top-down and bottom-up techniques.[1−5]

As an interesting morphology and phase, the 1D bicrystalline (twinned) nanostructures have received much consideration because of their peculiar structure.[6−9] Bicrystals are widely used in microelectronics for enhancing operation efficiency and acting as an intermediate phase during processing single Josephson's junctions and colossal magnetoresistance devices.[10,11] Twinned bicrystals generate positive energy and are expected to have important influence on the mechanical, electronic, and optical properties of a given material. For example, previous investigations reveal that a twin boundary can act as a natural potential well for electrons, thus inducing a two-dimensional (2D) electron system and resulting in different physical properties.[12] For a better understanding of the bicrystalline nanostructure performance, it becomes imperative to investigate the defect configurations down to the atomic level.[13]

In this work, novel bicrystalline Zn_3P_2 and Cd_3P_2 nanobelts were synthesized in a vertical induction furnace[14] via a one-

* To whom correspondence should be addressed. E-mail: guozhens@usc.edu (G.S.); chongwuz@usc.edu (C.Z.).
† University of Southern California.
‡ MANA, National Institute for Materials Science.
§ Nanoscale Materials Center, National Institute for Materials Science.

(1) (a) Yuan, J. K.; Li, W. N.; Gomez, S.; Suib, S. L. *J. Am. Chem. Soc.* **2005**, *127*, 14184. (b) Shen, G. Z.; Chen, D. *J. Am. Chem. Soc.* **2006**, *128*, 11762.
(2) (a) Liu, B.; Zeng, H. C. *J. Am. Chem. Soc.* **2004**, *126*, 8124. (b) Lao, J. Y.; Wen, J. G.; Ren, Z. F. *Nano Lett.* **2002**, *2*, 1287. (c) Liu, B.; Zeng, H. C. *Chem. Mater.* **2007**, *19*, 5824. (d) Zeng, H. C. *Int. J. Nanotechnol.* **2007**, *4*, 329.
(3) (a) Yan, H. Q.; He, R.; Pham, J.; Yang, P. D. *Adv. Mater.* **2003**, *15*, 402. (b) Wang, Z. L.; Kong, X. Y.; Zuo, J. M. *Phys. Rev. Lett.* **2003**, *91*, 185502.
(4) (a) Lu, W.; Gao, P.; Jian, W. B.; Wang, Z. L.; Fang, J. *J. Am. Chem. Soc.* **2004**, *126*, 14816. (b) Lu, W.; Ding, Y.; Chen, Y.; Wang, Z. L.; Fang, J. *J. Am. Chem. Soc.* **2005**, *127*, 10112.
(5) (a) Gudiksen, M. S.; Lauhon, L. J.; Wang, J. F.; Smith, D. C.; Lieber, C. M. *Nature* **2002**, *415*, 617. (b) Qian, F.; Li, Y.; Gradecak, S.; Wang, D.; Barrelet, C. J.; Lieber, C. M. *Nano Lett.* **2004**, *4*, 1975.
(6) (a) Wang, H.; Liu, G.; Yang, W.; Lin, L.; Xie, Z.; Fang, J.; An, L. *J. Phys. Chem. C* **2007**, *111*, 17169. (b) Xu, C.; Youkey, S.; Wu, J. F.; Jiao, J. *J. Phys. Chem. C* **2007**, *111*, 12490. (c) Xu, C.; Chun, J.; Rho, K.; Lee, H. J.; Jeong, Y. H.; Kim, D. E.; Chon, B.; Hong, S.; Joo, T. *Appl. Phys. Lett.* **2006**, *89*, 093117.
(7) (a) Jie, J.; Zhang, W.; Jiang, Y.; Meng, X. M.; Zapien, J. A.; Shao, M.; Lee, S. T. *Nanotechnology* **2006**, *17*, 2913. (b) Zou, K.; Qi, X.; Duan, X.; Zhou, S.; Zhang, X. *Appl. Phys. Lett.* **2005**, *86*, 013103. (c) Jiang, X. C.; Herricks, T.; Xia, Y. N. *Nano Lett.* **2002**, *2*, 1333.
(8) (a) Meng, X.; Jiang, Y.; Liu, J.; Lee, S. C.; Bello, I.; Lee, S. T. *Appl. Phys. Lett.* **2003**, *83*, 2244. (b) Tao, X.; Li, X. D. *Nano Lett.* **2008**, *8*, 505.
(9) (a) Yang, Y.; Sun, X. W.; Tay, B. K.; Wang, J.; Dong, Z.; Fan, H. *Adv. Mater.* **2007**, *19*, 1839. (b) Kim, H. W.; Shim, S. H. *Thin Solid Films* **2007**, *515*, 5158. (c) Shen, G. Z.; Bando, Y.; Liu, B.; Tang, C.; Golberg, D. *J. Phys. Chem. B* **2006**, *110*, 20129.
(10) (a) Mashtakov, A. D.; Konstantinyan, K. I.; Ovsyannikov, G. A.; Stephantsov, E. A. *Tech. Phys. Lett.* **1999**, *25*, 249. (b) Ataev, B. M.; Kamilov, I. K.; Mamedov, V. V.; Bagamadova, A. M.; Makhmudov, S. S. *J. Phys. D* **2001**, *34*, L46.
(11) Mathur, N. D.; Burnell, G.; Isaac, S. P.; Jackson, T. J.; Teo, B. S.; MacManus-Driscoll, J. L.; Cohen, L. F.; Evetts, J. E.; Blamire, M. G. *Nature* **1997**, *387*, 266.
(12) Tomaru, T.; Ohyama, T.; Otsuka, E.; Isshiki, M.; Igaki, K. *Phys. Rev. B* **1992**, *46*, 9390.
(13) (a) Arushanov, E. K. *Prog. Cryst. Growth Charact.* **1980**, *3*, 211. (b) Sieranski, K.; Szatkowski, J.; Misiewicz, J. *Phys. Rev. B* **1994**, *50*, 7331. (c) Andrzejewski, J.; Misiewicz, J. *Phys. Stat. Sol. B* **2001**, *227*, 515. (d) Ding, Y.; Wang, Z. L. *J. Phys. Chem. B* **2004**, *108*, 12280.
(14) (a) Gao, Y. H.; Bando, Y. *Nature* **2002**, *415*, 6872. (b) Shen, G. Z.; Bando, Y.; Hu, J. Q.; Golberg, D. *Appl. Phys. Lett.* **2007**, *90*, 123101. (c) Golberg, D.; Bando, Y.; Tang, C.; Zhi, C. *Adv. Mater.* **2007**, *19*, 2413.

10.1021/cm802516u CCC: $40.75
Published on Web 11/05/2008

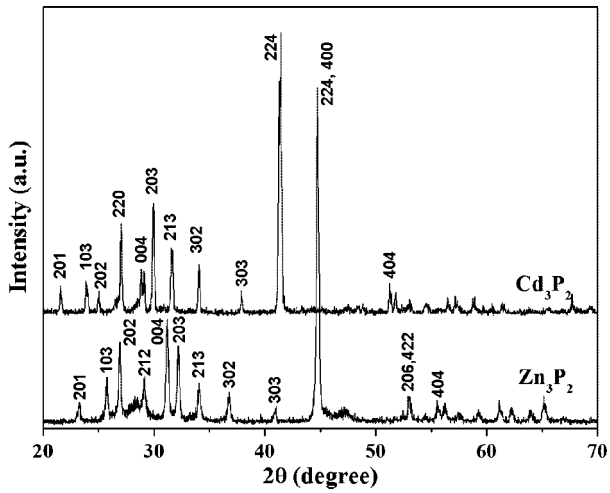

Figure 1. XRD patterns of the synthesized Zn_3P_2 and Cd_3P_2 products.

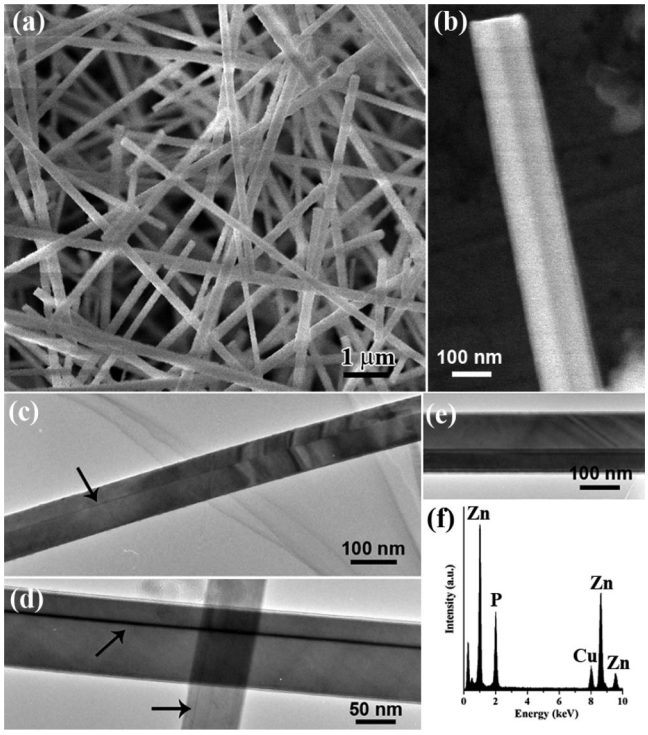

Figure 2. (a) SEM image of a Zn_3P_2 product. (b) High-magnification SEM image of a single bicrystalline Zn_3P_2 nanobelt, showing clear grain boundary along the growth direction. (c−e) TEM images of typical bicrystal Zn_3P_2 nanobelts. (f) EDS spectrum taken from the nanobelts.

step vapor-solid process without the use of any template or catalyst. Both the synthesized Zn_3P_2 and Cd_3P_2 nanobelts consist of two single-crystalline tetragonal Zn_3P_2 or Cd_3P_2 domains and have a growth axis along the [101] planes. Field-effect transistors (FETs) based on single bicrystalline Zn_3P_2 and Cd_3P_2 nanobelts were fabricated. The results show that both nanomaterials are of *p*-type and the thermal activation is the dominant transport mechanism in them. We choose Zn_3P_2 and Cd_3P_2 because, with important applications in infrared detectors, lasers, solar-cells, ultrasonic multipliers, Li-ion batteries,[15−18] etc., they represent a special class of II_3-V_2 narrow band gap semiconductors. Zn_3P_2 and Cd_3P_2 have a direct band gap of 1.51 and 0.55 eV, respectively.[15,16] Within a tetragonal phase, Zn^{2+} (or Cd^{2+}) is tetrahedrally coordinated with P atoms in Zn_3P_2 (or Cd_3P_2), whereas a P atom is surrounded by Zn^{2+} (or Cd^{2+}), located at six of the eight corners of a cube. The other two sites are at the diagonally opposite corners of a cubic face. The whole structure can be regarded as a tetra-fold superlattice of an antifluorite structure.[16] Considering large excitonic radii, quantum confinement of charge carriers in these two systems is much stronger and size-quantization effects are much more pronounced than in most of other II−VI and III−V semiconductors.

2. Experimental Section

Both bicrystalline Zn_3P_2 and Cd_3P_2 nanobelts were synthesized in a vertical induction furnace. The furnace consists of a fused quartz tube and an induction-heated cylinder made of high-purity graphite coated with a carbon-fiber thermo-insulating layer. Two inlet and one outlet graphite pipe were set on its top and base, respectively. In a typical process, a graphite crucible containing a mixture of Zn (or Cd), ZnS (or CdS), GaP, Mn_3P_2 with a molar ratio of 0.1:1:0.5:1 was loaded in the center of the heating zone. After evacuating the system to about 20 Pa, two flows of pure Ar were introduced into the furnace from the inlet pipes on the top and base, respectively. The flow rate was controlled to be 100 sccm from the top and 50 sccm from the base, respectively. After purging for 10 min, the crucible was rapidly heated to 1350 °C within 10 min and kept at that temperature for 60 min while the system was kept at ambient pressure. Dark-yellow (Zn_3P_2) and gray-black (Cd_3P_2) wool-like products were found deposited on the inner wall of the graphite crucible, which were collected for characterization by using XRD with Cu Kα radiation (λ=1.5418 Å, RINT 2200F), SEM (JEOL JSM-6700), and TEM (JEOL JEM-3000F) equipped with an energy-dispersive X-ray spectrometer (EDS).

3. Results and Discussion

After the syntheses, the inner wall of a crucible was covered with wool-like products. Figure 1 (bottom) shows an X-ray diffraction (XRD) pattern of a product from Zn, ZnS, GaP, and Mn_3P_2. All the strong peaks in this pattern can be indexed to tetragonal Zn_3P_2 (JCPDS 65−2854). No peaks from other impurities were found, indicating the formation of pure Zn_3P_2. As for the product from Cd, CdS, GaP, and Mn_3P_2, XRD pattern shown in Figure 1 (upper) reveals only peaks from tetragonal Cd_3P_2 (JCPDS No. 65−2856), also indicating the formation of a pure Cd_3P_2 phase.

Figure 2a is a scanning electron microscopy (SEM) image of a Zn_3P_2 product. Long and straight Zn_3P_2 nanobelts are clearly observed at high yield. Each nanobelt has a uniform width of 100−200 nm over its entire length, and a length in the range of tens of micrometers. Interestingly, a high-magnification SEM image, shown in Figure 2b, clearly reveals that a nanobelt possesses a distinct grain boundary along the direction parallel to the growth direction, indicating its bicrystal nature. The Zn_3P_2 nanobelts were also characterized using transmission electron microscopy (TEM) and the corresponding TEM images are depicted in Figures 2c−e. Clear grain boundaries are observed, as indicated with arrows in the images, confirming the SEM results. Several hundreds of nanobelts were analyzed and most of them have similar bicrystalline charac-

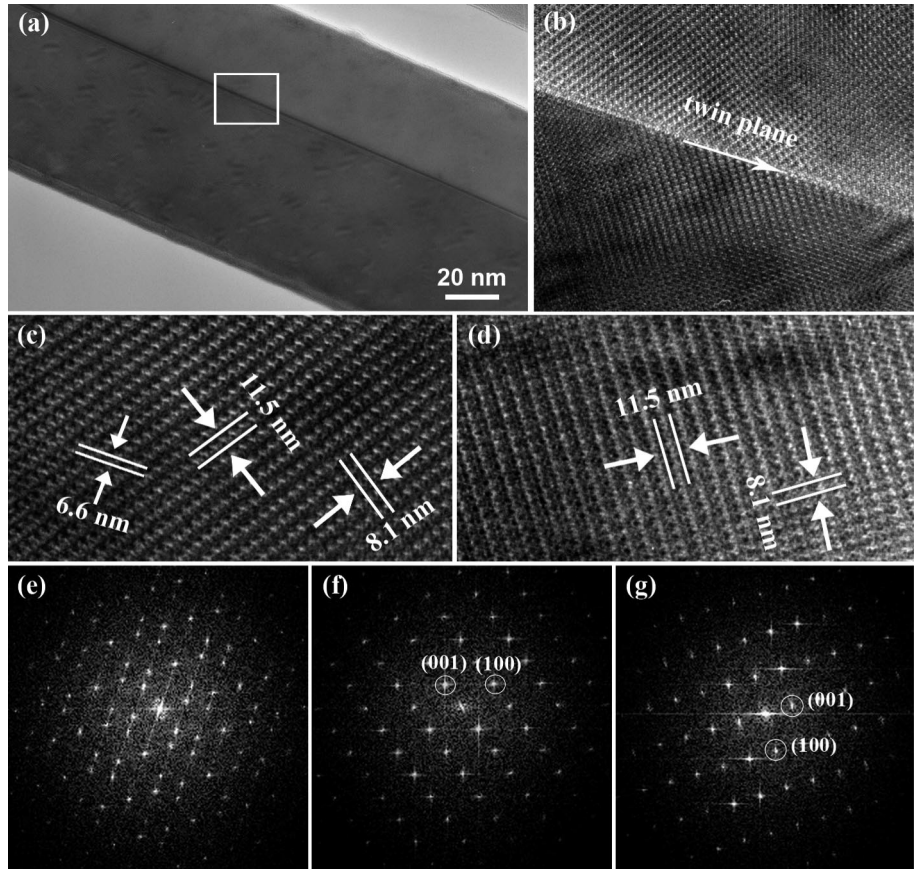

Figure 3. (a) TEM image and (b) HRTEM image of a bicrystalline Zn_3P_2 nanobelt. (c, d) Lattice-resolved HRTEM image taken from two parts of a Zn_3P_2 nanobelt. (e−g) FFT patterns taken from the whole bicrystalline Zn_3P_2 nanobelt and each part of it.

teristics. X-ray energy dispersive spectra (EDS) were taken to check the composition, the representative one is shown in Figure 2f. It shows the peaks of Zn, and P with a composition of ca. 3:2 stoichiometry, thus close to a Zn_3P_2, compound. No peaks from Mn or Ga were detected using EDS, indicating there are either no impurities or the concentration of Mn or Ga is lower than the EDS limitation.

The detailed microstructures of the Zn_3P_2 nanobelts were studied using high-resolution TEM (HRTEM). Figure 3a is a high-magnification TEM image of a bicrystalline Zn_3P_2 nanobelt, where two sides can be clearly seen due to the different brightness contrasts. An enlarged TEM image of the area marked with a square in Figure 3a is shown in Figure 3b. The twin plane of the nanobelt can be easily seen, as indicated with an arrow in the image. It also reveals that each side of the bicrystal nanobelt is, indeed, a single crystal. The lattice-resolved HRTEM images of both sides of the nanobelt are depicted in images c and d in Figure 3, respectively. The clearly resolved lattice fringes are 11.5 nm, 8.1 nm, and 6.6 nm. These correspond to the (001), (100), and (101) planes of tetragonal Zn_3P_2, respectively. Figure 3e−g shows the fast Fourier transform patterns corresponding to the nanobelt as a whole (Figure 3e) and its upper (Figure 3f) and lower parts (Figure 3g). The mirror-image relationship between the two sets of diffraction spots (Figure 3e) confirms the formation of a bicrystalline structure. FFT patterns of each part again confirm that both fragments are single crystals. Combining the HRTEM images and the FFT patterns, it is concluded that the bicrystalline Zn_3P_2 nanobelts are composed of two single-crystals with the preferred growth axis along the [101] directions.

Figure 4a is a SEM image of a Cd_3P_2 product, which is also composed of numerous wirelike nanostructures. A high-magnification SEM image depicted in Figure 4b shows that, actually, the wires are nanobelts with a uniform diameter of ca. 100−200 nm along the whole structure. Similar to Zn_3P_2 bicrystals, TEM images shown in Figures 4c and 4d reveal that each nanostructure also consists of two individual parts, in accord with the bicrystalline morphology. A selected-area electron diffraction (SAED) pattern taken from a Cd_3P_2 bicrystal is depicted in Figure 4e, the two sets of diffraction spots are clearly seen, revealing the twin relationship. An EDS spectrum of the nanobelts (Figure 4f) shows peaks of Cd and P with a composition close to Cd_3P_2. Similar to the Zn_3P_2 result, no peaks from Mn or Ga were detected. Figure 4g depicts a HRTEM image of a nanobelt. The marked lattice fringes for each part are 0.71 nm, corresponding to the (101) plane of tetragonal Zn_3P_2. Figures 4h and 4i correspond to the FFT patterns of the upper and bottom parts shown in Figure 4g. Both parts are single crystals. The results verified the formation of bicrystalline Cd_3P_2 nanobelts with the preferred growth axis along the [101] directions, similar to the case of Zn_3P_2.

To investigate the possible growth mechanism, controlled experiments were conducted under similar conditions except that different source materials were used. We found that the use of both Mn_3P_2 and GaP as the phosphorus source are

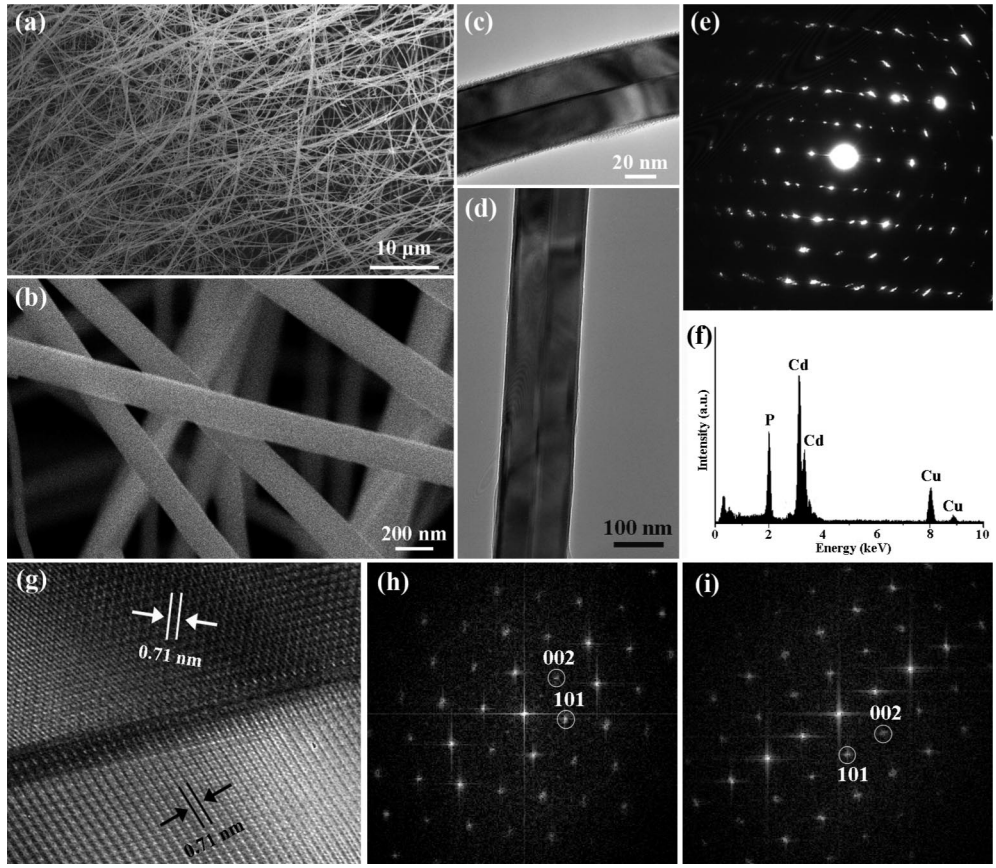

Figure 4. (a, b) SEM images of a Cd_3P_2 product at different magnifications. (c, d) TEM images of typical bicrystalline Cd_3P_2 nanobelts. (e) SAED pattern taken from a bicrystalline Cd_3P_2 nanobelt. (f) EDS spectrum of a Cd_3P_2 nanobelt. (f) HRTEM image and (g, h) its FFT patterns of a Cd_3P_2 nanobelt.

critical to form bicrystal nanowires in the experiments. If we used only Mn_3P_2 or GaP and kept other parameters constant, only single crystalline nanowires/nanobelts are obtained instead of bicrystal nanobelts. Recently, it was found that, by introducing impurities into the vapor phase reaction system, nanostructures with special shapes were formed. For example, ZnS bicrystal nanoribbons were formed at high temperature with the introduce of Si as impurities.[6,8] In the present work, a mixture of Zn (or Cd), ZnS (or CdS), GaP, Mn_3P_2 were used as source materials. Complicated reactions may occur during the experiments and the rapid heating rate, high vapor pressure, and impurities are believed to induce strain in the crystals in the initial stage. High concentration Ga and Mn vapors generated at high temperature during the reactions induce a lot of strains in the initial stage in a very short time, which is accumulated gradually during growth. Once reached up to a certain level, the strains will be relaxed and result in the formation of defective structures, such as stacking faults, which finally induced the formation of bicrystal structures, similar with previous reports on other bicrystal materials.[6−8] For example, bicrystal ZnO nanowires were formed at high yield in the presence of both Bi and Mn impurities, whereas only single-crystalline ZnO nanowires are formed in the presence of only Mn.[6b,c]

To study the electronic transport properties of the present nanobelts, we fabricated single-nanobelt-based field-effect transistors (FETs) along with the procedure previously described by us.[19] First, Zn_3P_2 and Cd_3P_2 bicrystalline nanobelts were sonicated in isopropanol. They

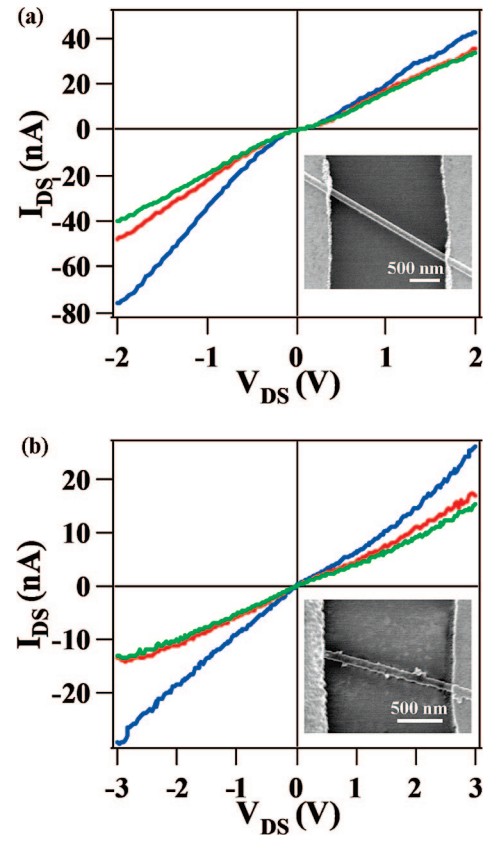

Figure 5. Gate-dependent $I-V$ curves of (a) Zn_3P_2 and (b) Cd_3P_2 nanobelts, showing the p-type characteristics for both devices. The insets show the SEM images of the setups.

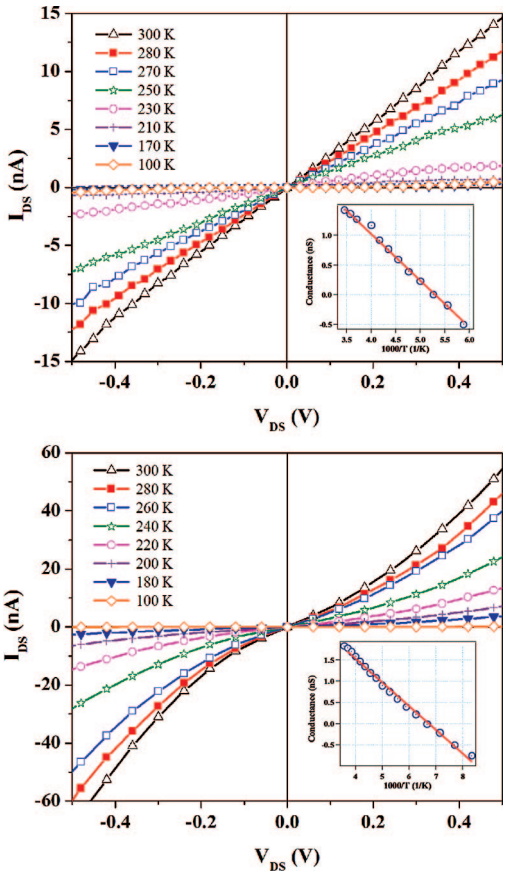

Figure 6. $I-V$ curves of (a) Zn_3P_2 and (b) Cd_3P_2 nanobelts measured at 300−100 K. The insets show the conductance in a logarithmic scale at zero bias voltage plotted as a function of 1000/T.

were then deposited onto a degenerately doped silicon wafer covered with a 500 nm thick amorphous SiO_2 layer. After the the nanobelts were dried in air, photolithography was performed, followed by the Ti/Au drain and source contacts deposition on both nanostructure ends. The Figure 5a inset is a SEM image of a Zn_3P_2 nanobelt device. It has a channel length of 2 μm. Figure 5a shows the gate-dependent current−voltage ($I-V$) curves obtained from a Zn_3P_2 nanobelt. Linear current (I_{ds}) versus voltage (V_{ds}) was observed, indicating the Ohmic contacts to the structure. With a negatively increasing gate voltage (0−30 V), the conductance of the device gradually increases, indicating a p-type transistor. The gate effect is rather weak, which is believed to be caused by the existence of high density defect sites within the nanobelts. The gate-dependent $I-V$ curves of a bicrystalline Cd_3P_2 nanobelt transistor were also investigated and the curves are depicted in Figure 5b. The applied gate voltages range from −30 to 30 V. It can be seen that they show very similar behaviors compared with the Zn_3P_2 transistors, that is, the p-type characteristics. A SEM image inset in Figure 5b demonstrates the Cd_3P_2 device with a channel length of about 1.5 μm.

The electronic properties of fabricated devices were explored as a function of temperature in vacuum. Figure 6a displays the $I-V$ curves of a Zn_3P_2 device measured from 300 to 100 K, without applying a gate voltage. It can be seen that the conductance of the device decreases monotonically as the temperature decreases. The zero-bias conductance was calculated to be 27.75 nano-Siemens (nS) at 300 K, whereas it decreased significantly to 0.01 nS at 100 K. The Figure 6a inset is a plot of the zero-bias conductance in a logarithmic scale as a function of 1000/T. This shows the linear behavior within the temperature region studied. It is known that the conductance versus temperature of a semiconducting device can be fitted as $G \approx \exp(-E_\alpha/K_BT)$. The calculated E_α is 159.7 meV. The results suggest that the thermal activation of carriers is the dominant transport mechanism for the Zn_3P_2 nanodevice. This statement is in line with previous expectations and experiments.[20]

The $I-V$ curves as a function of temperature (100−300 K) for a Cd_3P_2 nanobelt device measured in vacuum are shown in Figure 6b. The $I-V$ curves display similar character as those of the Zn_3P_2 case. The calculated zero-bias conductance for the Cd_3P_2 device is about 54.01 nS at 300 K and decreases to 0.05 nS at 100 K. The plot shown in the Figure 6b inset is the zero-bias conductance in a logarithmic scale as a function of 1000/T. Linear behavior is apparent, similar to the Zn_3P_2 device. Thus the thermal activation of carriers is also verified as the dominant transport mechanism for the latter device. The calculated E_α is about 110 meV.

4. Conclusion

In conclusion, novel bicrystalline Zn_3P_2 and Cd_3P_2 nanobelts were synthesized via a one-step vapor-solid process. The nanobelts of both systems consist of two single-crystalline twinned tetragonal domains and have the growth axes along the [101] planes. p-Type field-effect transistors (FETs) based on single Zn_3P_2 and Cd_3P_2 nanobelts were fabricated. Those revealed the thermal activation of carriers as the dominant transport mechanism, as was verified under the measurements at various temperatures (100−300 K).

Acknowledgment. The authors acknowledge financial support from the L.K. Whittier Foundation, and the National Science Foundation (CCF-0726815 and CCF-0702204).

CM802516U

(15) (a) Zdanowicz, W.; Zdanowicz, L. *Annu. Rev. Mater. Sci.* **1976**, *5*, 301. (b) Larzarev, V. B.; Schevchenka, V. Y.; Greenberg, Y. H.; Sobolein, V. V. *II−V Semiconducting Compounds*; Nauka: Moscow, 1978.

(16) (a) Buhro, W. E. *Polyhedron* **1994**, *13*, 1131. (b) Green, M.; O'Brien, P. *Chem. Mater.* **2001**, *13*, 4500. (c) Green, M.; O'Brien, P. *J. Mater. Chem.* **1999**, *9*, 243. (d) Zhao, X.; Shi, J. L.; Hu, B.; Zhang, L. X.; Hua, Z. L. *J. Mater. Chem.* **2003**, *13*, 399.

(17) (a) Pawlikowski, J. M. *Infrared Phys.* **1988**, *28*, 177. (b) Bichat, M. P.; Pascal, J. L.; Gillot, F.; Favier, F. *Chem. Mater.* **2005**, *17*, 6761. (c) Bhushan, M. *Appl. Phys. Lett.* **1982**, *1*, 51. (d) Bhushan, M.; Catalano, A. *Appl. Phys. Lett.* **1981**, *38*, 39.

(18) (a) Fagen, E. A. *J. Appl. Phys.* **1979**, *50*, 6505. (b) Li, Y. *Phys. Status Solidi B* **1989**, *153*, 215.

(19) (a) Liu, X.; Li, C.; Han, S.; Han, J.; Zhou, C. *Appl. Phys. Lett.* **2003**, *82*, 996. (b) Liu, Z.; Zhang, D.; Han, S.; Li, C.; Tang, T.; Jin, W.; Liu, X.; Lei, B.; Zhou, C. *Adv. Mater.* **2003**, *15*, 1754. (c) Li, C.; Zhang, D.; Han, S.; Liu, X.; Tang, T.; Zhou, C. *Adv. Mater.* **2003**, *15*, 143.

(20) (a) Liu, X.; Li, C.; Han, S.; Han, J.; Zhou, C. *Appl. Phys. Lett.* **2003**, *82*, 1950. (b) Zhou, C.; Kong, J.; Dai, H. *Appl. Phys. Lett.* **2000**, *76*, 1597.